Journal of Structural Geology 33 (2011) 1715–1727

Contents lists available at SciVerse ScienceDirect

Journal of Structural Geology

journal homepage: www.elsevier.com/locate/jsg

Review article

Exploring fault rocks at the nanoscale

Cecilia Viti*

Earth Science Department, University of Siena, Via Laterina 8, 53100 Siena, Italy

ARTICLE INFO

Article history:
Received 22 July 2010
Received in revised form
7 October 2011
Accepted 11 October 2011
Available online 21 October 2011

Keywords:
Ultrafine fault rocks
Clays
Mineral weakening
Mineral reaction
Nanostructures
TEM

ABSTRACT

This paper aims to demonstrate the potential role of micro/nanoscale investigations in the study of fault rocks, given that a multiscale and multidisciplinary approach linking structural geology, petrology and mineralogy from the outcrop to the unit-cell scale is essential to the comprehensive characterization of geological materials. To explore fault rocks at the sub-micrometer scale, a fundamental contribution is provided by the Transmission Electron Microscope (TEM), which offers a real-time combination of high-resolution images, diffraction patterns, and chemical data for extremely small volumes, providing accurate mineralogical and nanostructural determinations.

This paper focuses on a few selected examples, that are particularly appropriate for TEM investigation, in particular: 1) grain-size determinations on ultrafine-grained fault rocks; 2) detection and characterization of poorly crystalline minerals (e.g., clays) and amorphous phases within fault rocks; 3) identification of deformation-induced mineral reactions occurring within fault zones (e.g., dolomite decarbonation and serpentine dehydration); and 4) observations of recurrent deformation nanotextures in phyllosilicates. TEM investigation can provide an unexpected amount of data, much of which cannot be obtained by conventional techniques, and it can therefore significantly contribute to an understanding of the physico-chemical conditions for faulting and fault mechanics.

1. Introduction

A fault zone is an extremely dynamic system, characterized by specific physico-chemical conditions that typically result in enhanced mineral reactivity and intense microstructural changes. Consequently, rocks that form within a fault zone are among the most complex and heterogeneous geological materials, and their comprehension requires a multidisciplinary and multiscale investigation, from the outcrop to the single-crystal scale. The characterization of a fault rock can be achieved through the identification of 1) fault-rock mineralogy and microstructure, which in most cases, differ from the original protolith; 2) the nature of deformation-induced and deformation-facilitated reactions, which are fundamentally controlled by specific geodynamical and physico-chemical conditions, such that even opposite processes (e.g., hydration versus dehydration or crystallization versus amorphization) may be favoured in different fault zones; and 3) the way that fault rock with specific mineralogical and microstructural characteristics behaved during deformation, from microstructural evidence of deformation mechanisms and strain partitioning.

The accurate characterization of these features within a fault-rock sample is commonly complicated by the development of poorly crystalline to amorphous phases and ultrafine grained mineral assemblages (e.g., Yund et al., 1990; Di Toro et al., 2004; Chester et al., 2005; Solum et al., 2005; Schleicher et al., 2011 and references below), which are difficult to investigate by conventional tools such as optical microscopy, scanning electron microscopy (SEM) and X-ray diffraction (XRD) techniques. XRD can tell us which minerals occur in a fault rock and in what amounts, providing both qualitative and quantitative mineralogical determinations. This approach is usually restricted to crystalline phases, even though specific methods, mostly based on XRPD full-profile Rietveld refinements, can detect and quantify also amorphous materials (e.g., Chipera and Bish, 2002). However, XRD does not provide direct microstructural determinations, including spatial distribution of the different minerals, grain size and grain size distribution, crystal habit, preferred orientation, grain-boundaries relationships, deformation microstructures, composition and spatial distribution of possible amorphous phases.

SEM investigation, coupled with microanalytical techniques, provides microstructural details, but it can suffer of at least two main drawbacks: 1) resolution limits, even if greatly improved by using field-emission-gun, FEG, instruments; and 2) the lack of crystal-structural information (i.e., diffraction data). Basically, the

* Tel.: +39 577 233988; fax: +39 577 233938.
E-mail address: vitic@unisi.it.

0191-8141/$ – see front matter © 2011 Elsevier Ltd. All rights reserved.
doi:10.1016/j.jsg.2011.10.005

last point means that nanosized quartz, coesite, opal and amorphous silica are difficult to distinguish. This also applies to ultracataclasites and pseudotachylyte glasses that are characterized by the same average chemical composition.

The TEM is the only instrument that provides high-resolution images, chemical analyses and diffraction data from submicrometric volumes simultaneously. For that reason, a growing number of studies of naturally and experimentally deformed rocks employ high-resolution and analytical TEM (e.g., Wibberley, 1999; Andreani et al., 2005; Escartin et al., 2008; and references below). Among the most commonly addressed topics are the characterization of ultrafine grained fault rocks, the identification and spatial distribution of poorly crystalline minerals (such as clays) and amorphous phases, the nature of deformation-induced nanostructures and mineral reactions. As detailed in the next sections, these features are important for the comprehensive knowledge of 1) the fault rock strength by accurate determinations of fracture surface energy (e.g., Wilson et al., 2005; Chester et al., 2005); 2) the dominant deformation mechanisms, with particular attention to fault weakening processes such as powder lubrication and mineral weakening (e.g., Han et al., 2010 and Schleicher et al., 2011, respectively); and 3) the fault rock genetic mechanisms and the physical-chemical conditions of faulting (e.g., De Paola et al., 2011; Viganò et al., 2011).

In this paper, I aim to emphasize the potential role of the TEM in the study of fault rocks, using case histories of broad geological interest to illustrate that TEM can provide data relevant to structural problems. Due to the extreme variability of fault rocks and related issues, and to the multiplicity of TEM experimental modes (e.g., bright versus dark field imaging), this review will be necessarily incomplete. In particular, to avoid too broad a scope, I will limit its scope to bright field TEM observations and to predominantly brittle deformation in the upper crust. To facilitate communication, the next section reports a short overview of TEM principles, providing a key for "reading" TEM images and diffraction patterns.

2. The transmission electron microscope

The transmission electron microscope (TEM) has a great and not yet fully explored potential in structural geology investigations. As a "microscope", it obviously provides enlarged views of the investigated object, with magnification up to ~1,000,000 times and theoretical point-to-point resolution close to 1 Å. The basic equipment is comparable to a petrographic optical microscope, upside down. The "light" source is located at the top of the microscope column and produces an incident electron beam that is accelerated downward and focussed, through the condenser lens system, onto the electron-transparent specimen, which must be thinner than 100 nm. The electrons emerging from the specimen are received by the objective lens and transferred, through the intermediate and projector lens system, downward to the viewing plane. However, by suitably changing the electrons' path across the intermediate and projector lenses, electron diffraction patterns can be obtained instead of images. "Switching" from images, referred to as direct space, to diffraction patterns, referred to as reciprocal space, is instantaneous. The addition of energy dispersive spectrometers (EDS) and other detectors, such as electron energy loss spectrometers (EELS), provides complementary chemical data.

Thus, the TEM is a powerful tool that produces high magnification images, and, at the same time, electron diffraction patterns and chemical analyses for extremely small volumes, that are several orders of magnitude smaller than can be analysed using conventional X-ray diffraction and spectrometry. The real-time combination of electron images, diffraction patterns and chemical data with high spatial and analytical resolution is probably the most outstanding feature of this instrument, making it an indispensable tool in the study of heterogeneous, ultrafine grained and poorly crystalline materials, such as fault rocks frequently are.

The interpretation of TEM images is not straightforward, depending on several parameters including microscope operating conditions (e.g., magnification, astigmatism, defocus value), sample variables (e.g., sample thickness, crystal orientation, beam damage) and imaging modes (e.g., bright versus dark field, amplitude versus phase contrast images). In this paper, I will only deal with bright-field phase-contrast images, neglecting the huge contribution of dark-field imaging to the study of crystal deformation, particularly for dislocation geometry, distribution and evolution (e.g., Christie and Ardell, 1976; Green, 1992). The interpretation of electron diffraction patterns is also complex, requiring basic knowledge of diffraction theory and the concept of reciprocal space. For the purposes of this paper, the readers should keep in mind that any crystalline material, consisting of regularly spaced hkl planes (direct lattice), gives rise to regularly spaced diffracted reflections (reciprocal lattice), each of which is generated by a single hkl plane. The measure of periodicities in the reciprocal lattice (i.e., in the experimental diffraction pattern) allows the determination of the interplanar distances d_{hkl} and, consequently, the unequivocal identification of any diffracting crystalline phase. For example, the (001) basal planes of phyllosilicates would produce a single 001 diffraction spot (e.g., Fig. 1a); planes (002), (003), (004) would produce a spot each, all aligned along the same direction, i.e., along the reciprocal axis $[00l]^*$ (or c^*). The measure of the c^* axis periodicity allows the determination of the interplanar distance d_{001}, which is a distinguishing characteristic of the different phyllosilicates.

Fig. 1 shows representative electron diffraction patterns, obtained with a parallel incident beam from selected portions of a given specimen using the selected-area electron diffraction (SAED) technique. The examples illustrate the use of diffraction patterns to unequivocally determine the mineralogy of ultrafine grained fault rocks on the basis of measured d_{hkl}, as well as to distinguish amorphous from poorly or highly crystalline materials. The first example (Fig. 1a) is a SAED pattern of a biotite single crystal that was tilted and suitably oriented under the electron beam. The main reciprocal axes (arrows) in this orientation are b^* and c^* (diffraction spots are indexed accordingly), with c^* periodicity corresponding to ~10 Å lattice spacing which is typical of 1 M polytypes in micas. The diffraction spots are particularly sharp and intense, indicating high crystallinity and structural order. Fig. 1b shows the SAED pattern of a talc single crystal in its a^*c^* orientation (c^* periodicity ~9 Å). The most evident difference with respect to the previous SAED pattern is that diffraction spots are diffuse and streaked along c^*. This feature, common in layer silicates, is indicative of irregular layer stacking, due to polytypic disorder of the same phyllosilicate or to irregular intergrowth of different phyllosilicates with variable d_{001}. Fig. 1c, also from a talc sample, is an example of SAED pattern where several crystals are in slightly variable orientations, as testified by the angular divergence among corresponding c^* axes and by the formation of diffraction "arcs". A similar pattern can be produced by a fold in a phyllosilicate grain. When the diffracting volume consists of a large number of crystals in completely random orientations, the corresponding SAED pattern is ring-shaped (e.g., Fig. 1d). Measurements of ring radii provide a list of d_{hkl} interplanar distances, equivalent to the d_{hkl} lists obtained by X-ray powder diffraction experiments. Ring-shaped patterns (e.g., Fig. 1d) can, however, be produced by both ultrafine-grained cataclasites and randomly oriented new grains crystallized within a fault zone. This fact emphasizes that SAED patterns must always be interpreted within a broader context, coupling diffraction data with images and chemical data.

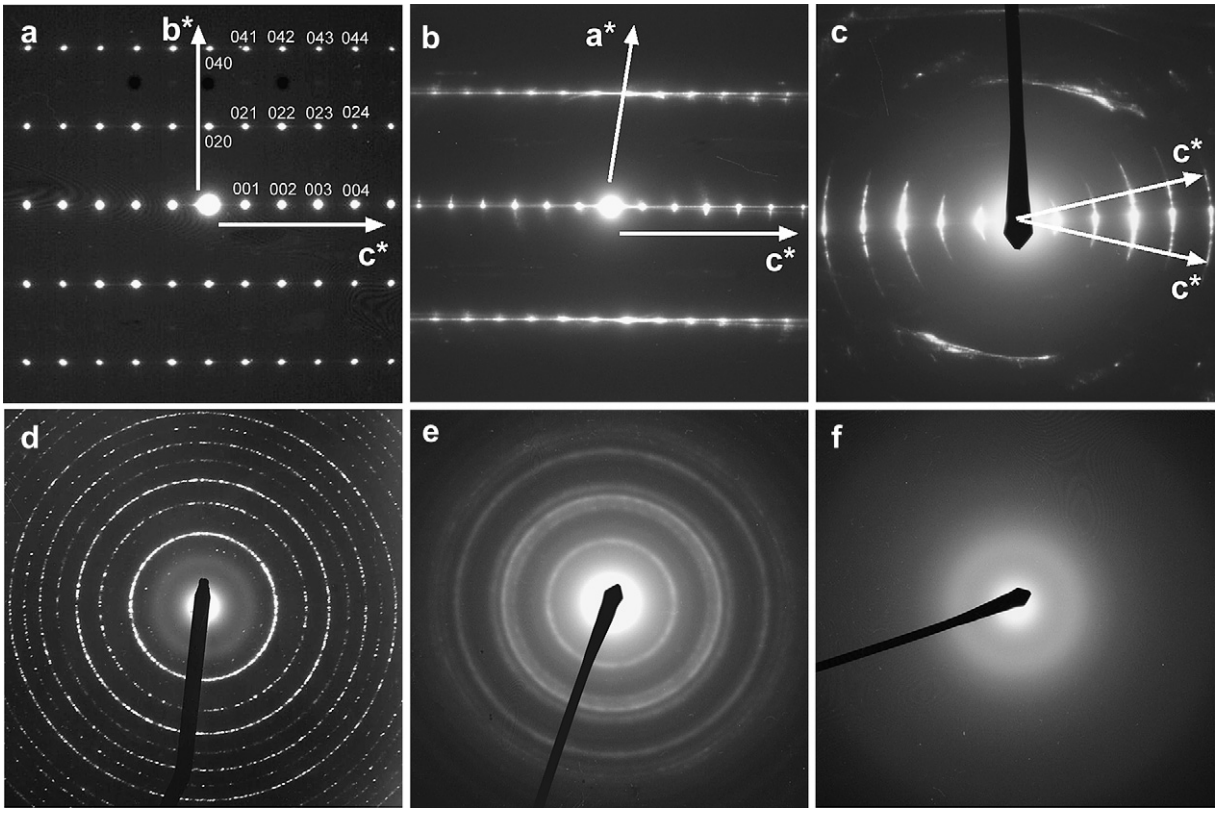

Fig. 1. Representative selected area electron diffraction (SAED) patterns. In each, the central intense spot corresponds to the unscattered, transmitted beam. (a) SAED pattern of a biotite single crystal (b*c* reciprocal plane), with sharp and intense spots. Arrows indicate the direction of the reciprocal axes b* and c*; reflections are indexed accordingly. (b) SAED pattern of a talc single-crystal (a*c* reciprocal plane), with c* streaking indicative of layer stacking disorder. (c) SAED pattern produced by slightly misoriented talc lamellae. (d) Ring-shaped SAED pattern produced by a polycrystalline sample, with randomly oriented grains. (e) Diffuse and weak ring-shaped SAED pattern produced by randomly oriented, poorly crystalline grains. (f) SAED pattern of an amorphous material, with diffuse scattering around the transmitted beam.

The ring-shaped SAED pattern in Fig. 1e is also produced by a polycrystalline and randomly oriented sample, but rings are diffuse and less intense, suggesting lower crystallinity with respect to the previous example. When the analysed volume does not have a crystalline structure (as in the case of glasses or other amorphous materials), the diffraction process does not occur and the corresponding SAED pattern will be just characterized by diffuse scattering around the transmitted beam (e.g., Fig. 1f).

Fig. 2 includes four examples of bright-field phase-contrast TEM images for deformation structures, obtained by combining the transmitted beam with an appropriate number of diffracted beams, as a function of the microscope theoretical resolution. Fig. 2a and b are low magnification images, particularly suitable for nanostructural analysis of characteristics such as crystal size and shape, size distribution, grain boundary character, porosity and crystallographic preferred orientation. Fig. 2a is a 30,000× magnified image showing an assemblage of rounded nanosized grains, typically 200 nm in diameter, in random orientations, consistent with corresponding ring-shaped SAED pattern (inset). Differences in grain contrast relate to variable crystal orientation and/or to variable sample thickness. In this kind of TEM image, pores appear white (arrows), corresponding to the maximum dose of transmitted unscattered electrons. Fig. 2b (original magnification of 40,000×) shows a different sample, predominantly formed by nanosized lamellar crystals that are kinked. The effect of kinking is evident in the corresponding SAED pattern (inset), which shows variably oriented c* axes. The angle between c* axes is equal to the kink angle. Fig. 2c and d are representative examples of lattice and high-resolution TEM images, respectively. Fig. 2c shows a detail of a lizardite crystal (planar serpentine), characterized by regularly stacked $(001)_{liz}$ lattice fringes (the NE-trending bright/dark thin lines), with stacking periodicity of approximately 7 Å (corresponding SAED pattern in the inset). The broad white features, parallel to $(001)_{liz}$, correspond to cleavage and interlayer delamination. Close to cleavage surfaces, the lizardite structure is typically affected by local bending of $(001)_{liz}$ lattice fringes and by partial amorphization (contrast-free arrowed portions). Fig. 2d shows a high-resolution detail of lizardite in the b*c* orientation. The bi-dimensional resolution (i.e., of both b and c periodicities) allows the determination of the stacking vector of (001) planes, here characterized by disordered polytypic sequences, as shown by the double white line which changes orientation where the stacking order changes.

In the proper original orientation, (hkl) lattice planes (direct space) are perpendicular to corresponding [hkl]* axis (reciprocal space). Thus, (001) lattice fringes of phyllosilicates should be perpendicular to the c* reciprocal axis. Unfortunately, due to editorial reasons, TEM images and corresponding SAED patterns are often rotated during figure assembly. For example, $(001)_{liz}$ lattice fringes in Fig. 2c should be rotated by ~ 30° anticlockwise. The correct indication of lattice fringes and reciprocal axes, however, overcomes this drawback.

The principles of TEM electron diffraction, imaging and spectroscopy are summarized by Wenk (1976), McLaren (1991) and Buseck (1992), which provide numerous examples from the geosciences, and by Williams and Carter (1996). This last reference also includes a useful summary of the main methods of TEM sample preparation ("This is the most tedious aspect of all TEM work…"

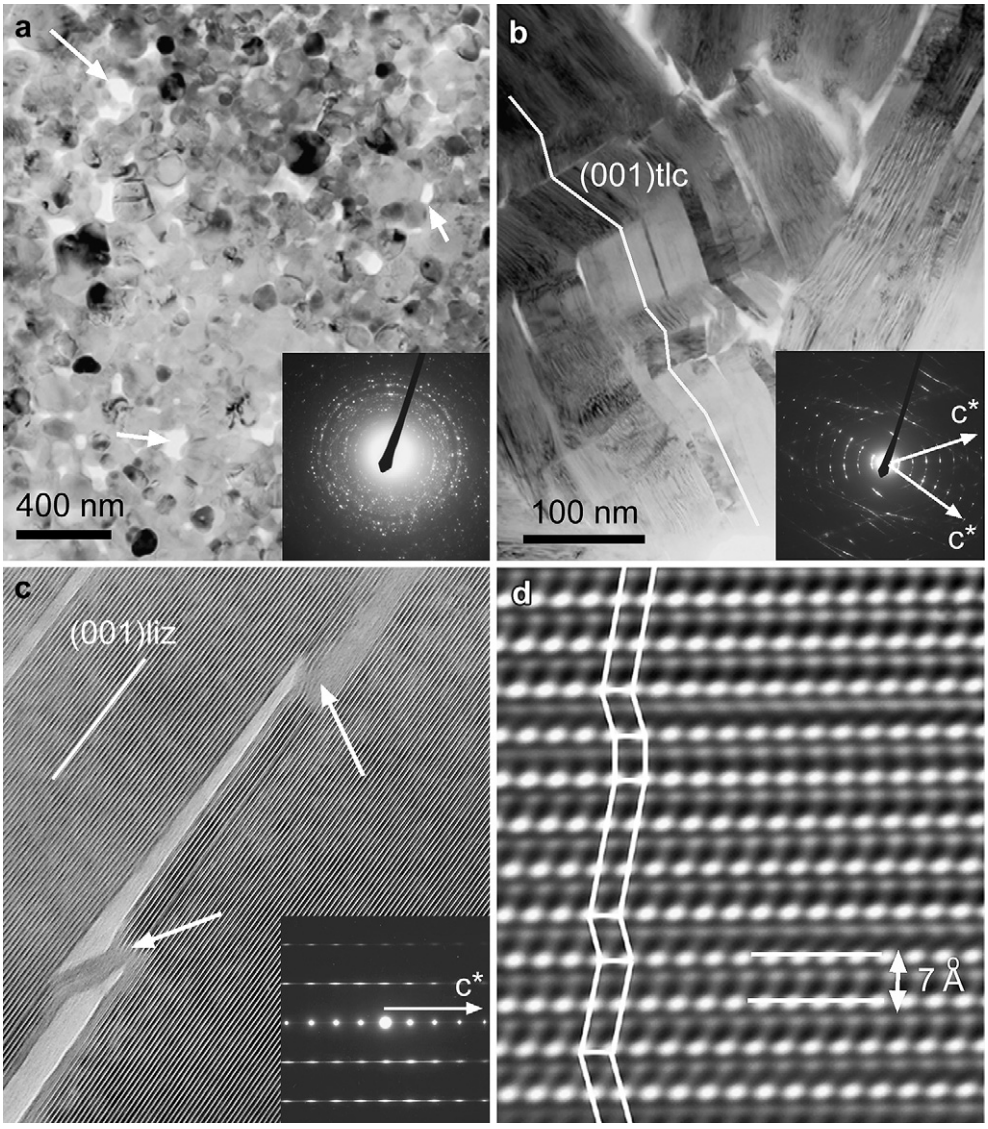

Fig. 2. (a) TEM image of an ultrafine assemblage of randomly oriented crystalline forsterite and enstatite. Arrows point to pores. The sample comes from the slip zone of an experimentally deformed serpentinite (high-velocity rotary experiment; Viti and Hirose, 2010). (b) Kinking in nanosized talc lamellae and corresponding SAED pattern (inset). White lines highlight the changes in the orientation of $(001)_{tlc}$ planes across kink axial planes (sample from the Zuccale fault). (c) Lattice fringe TEM image and corresponding SAED pattern (inset) of a lizardite crystal showing interlayer cleavage associated with local bending and amorphization. The thin SW-NE bright/dark lines correspond to 7 Å spaced (001) planes of lizardite. The sample comes from an experimentally deformed serpentinite (high-T torsion deformation; Viti and Hirose, 2009). (d) High-resolution TEM image of a lizardite crystal (b*c* orientation) from the same sample. Deformation-induced polytypic disorder produced the c* streaking in the corresponding SAED pattern (c); the double white line highlights the random orientation of the stacking vector.

and "The quality of your data is at least directly proportional to the quality of your specimen…"). Details on the focussed ion beam (FIB) technique (not treated by Williams and Carter, 1996) can be found in Wirth (2004).

3. Examples of TEM application to the study of fault rocks

Fault-rock-related features for which TEM study is particularly appropriate include 1) ultrafine-grained fault rocks, 2) poorly crystalline and amorphous phases within fault rocks, 3) deformation-induced mineral reactions within fault rocks, and 4) deformation-induced nanostructures (limited to layer silicates). Often, a fault-rock sample contains more than one of these features, so that they can be investigated simultaneously. Representative TEM observations from previous studies are shown, but their implications in structural geology are extensively detailed in the Discussion and Conclusions section.

3.1. Size determinations of fine and ultrafine grained materials

The TEM can be considered as an extended petrographic tool for the study of fine and ultrafine (below 100 nm) grained rocks. This important target in structural geology studies reveals ultrafine assemblages, that form in natural and experimental slip zones due to either extreme grain-size reduction, e.g., ultracataclasites (Sibson, 1977; Storti et al., 2003), or syn/post-dynamic crystallization of new mineral phases (e.g., De Paola et al., 2011). Ultrafine grained particles are observed in both large and small displacement fault zones, and in experimentally deformed samples, indicating that they are produced in a range of stress regimes. Chester et al. (2005) investigated the ultracataclasite layer of the Punchbowl

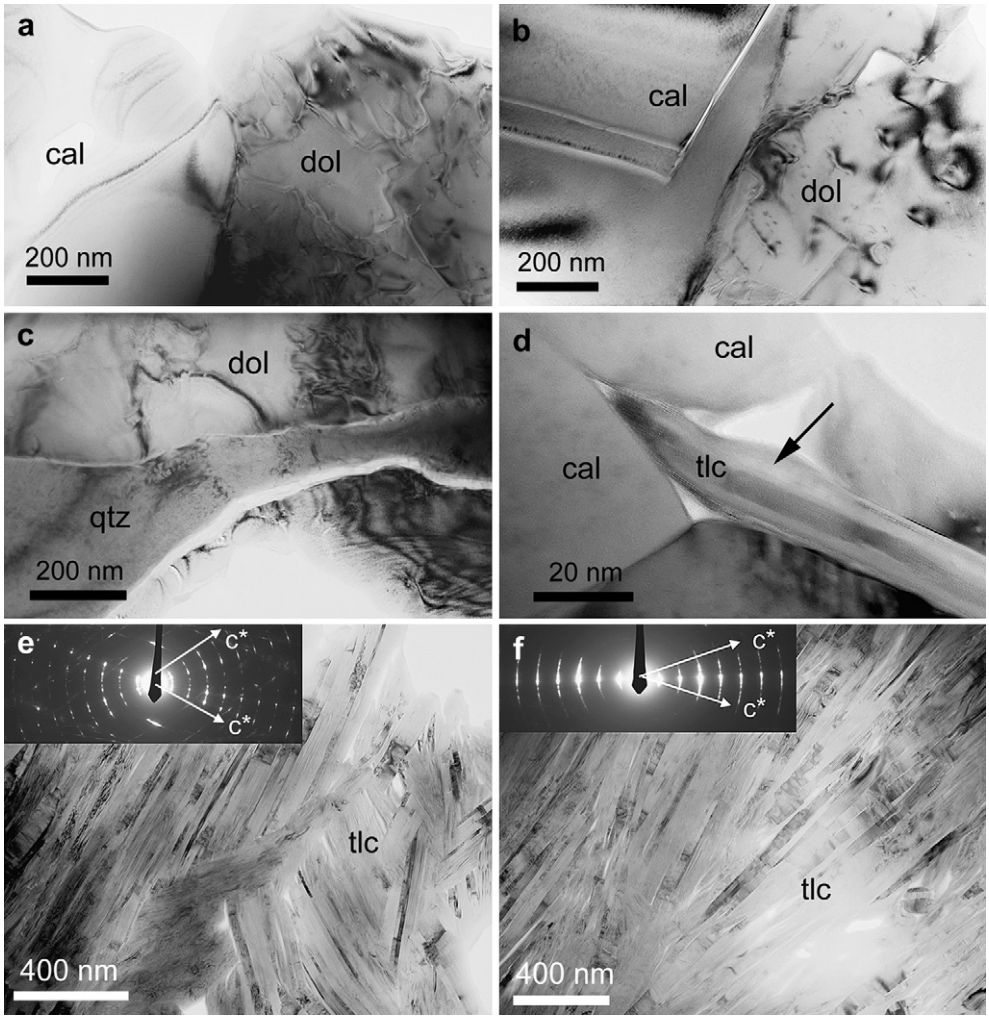

Fig. 3. TEM images recording dolomite breakdown in the Zuccale fault, with formation of calcite and talc. (a) and (b) Bright-field TEM images showing associated dolomite (dol) and calcite (cal); dolomite crystals are affected by strain contrast features (dark contrast), that are absent in nearby calcite crystals. (c) Dolomite-hosted silica vein, exhibiting ultrafine-grained and randomly oriented quartz crystals (qtz). (d) Early talc (tlc) at calcite/dolomite grain boundaries. Talc lamellae are associated with amorphous material (arrow). (e) and (f) Ultrafine talc lamellae in variably oriented and relatively well oriented nanostructures, respectively. Corresponding SAED patterns (insets) show higher and lower angular divergence among c* reciprocal axes, respectively.

fault, finding particles with a fractal size distribution from 40 μm to 50 nm, associated with smaller particles down to 4 nm in size. Dewers et al. (2003) employed the TEM to check the particle size distribution (PSD) of the sub-micrometer fraction of gouges from the San Andreas fault (~160 km slip) and from a recent seismic fault in South Africa (~0.4 m slip), finding that the fractal nature of many gouges could actually result from agglomeration of finer fragments rather than from comminution processes. Yund et al. (1990), Viti and Hirose (2010), Han et al., 2010 and De Paola et al. (2011) documented the common occurrence of ultrafine grains in experimentally deformed samples, whereas Janssen et al. (2011) used the TEM to investigate the ultrafine porosity of SAFOD (San Andreas Fault Observatory at Depth) core samples, finding pores with variable size (50–200 nm) and shape depending on fault rock fabric and alteration (note that TEM specimens were prepared by FIB to preserve pristine porosity).

These studies emphasize that, when ultrafine-grained fault rocks are concerned, unbiased grain size and PSD determinations with distinction between fractal and non-fractal distributions, can be achieved only by TEM investigations. High-magnification images reveal possible aggregation, cementation and healing processes, which are hardly detectable by optical microscopy and SEM, minimizing biased observations and, possibly, wrong genetic and mechanical interpretations. For example, Wibberley (1999) documented a cementation process within a quartz-feldspatic ultracataclasite, that caused fault-rock hardening. The cementation process was interpreted as due to the formation of new quartz nanograins, that were distinguished from pre-existing quartz clasts on the basis of TEM characteristics. This is clearly shown in Fig. 2d of the Wibberley paper, where highly dislocated clasts are closely associated with strain-free, neoformed grains. TEM images may also reveal the occurrence of intracrystalline defects, subgrain boundaries and poorly crystalline to amorphous coatings (Kennedy and Logan, 1998; Wibberley, 1999; Chester et al., 2005; Schleicher et al., 2011). For example, Fig. 3a in Chester et al. (2005) shows that nanoparticles in the Punchbowl fault ultracataclasite are pervasively lined by an ultrathin, poorly crystalline, lamellar material, which probably has a role in overall mechanical behaviour. Furthermore, the simultaneous availability of EDS chemical data and SAED patterns of the single nanoparticle allows confident mineral identification of ultrafine-grained polymineralic assemblages. The mineralogy of nanoparticles and, more specifically, the comparison between fault-rock and host-rock parageneses may usefully constrain the understanding of the fault-rock genetic

mechanism. For example, this kind of determinations allows straightforward distinction between extreme comminution, where the same mineralogical composition occurs in both host and fault rocks, vs. syn/post dynamic crystallization of new phases, where mineralogical composition differs.

The detection and the nanostructural characterization of ultrafine-grained materials are key to the study of fault rocks, because most mechanical, physical and chemical processes in a fault zone are grain-size sensitive and dependent on the grain-surface area. In particular, as detailed in the Discussion section, the fine and ultrafine fractions are believed to fundamentally influence fault-slip mechanisms, earthquake energy budget and fault-rock reactivity (e.g., Brodie and Rutter, 1987; Wilson et al., 2005; Carpinteri and Paggi, 2005; Chester et al., 2005; Liu and Cao, 2006; Sammis and Ben-Zion, 2008; Han et al., 2010, 2011).

3.2. Characterization of poorly crystalline and amorphous materials

As noted above, fault rocks may consist of ultrafine particles. The study of fault rocks can be further complicated by the occurrence of poorly crystalline and amorphous phases, often localized in micrometric or sub-micrometric horizons, films and coatings. X-ray diffraction techniques are generally insufficient to characterize these samples, due to the low intensity of diffracted beams and, most importantly, to the loss of microstructural relationships.

SEM with EDS or EMPA (electron microprobe analyses) provides textural and "bulk" chemical data on micrometer-sized volumes, but they do not yield in-situ characterizations of the crystal-structural state, i.e., they are not able to discriminate among crystalline materials with high structural order, disordered poorly crystalline materials or completely amorphous phases.

A significant example of poorly crystalline material common in fault rocks, is represented by clays. As detailed in the Discussion section, clays have important implications in fault strength and, specifically, in mineral weakening processes. The most common clays are illite ($d_{001} \sim 10$ Å), smectite ($d_{001} \sim 14$–20 Å, usually collapsed to 10 Å due to microscope high vacuum conditions), caolinite ($d_{001} \sim 7$ Å), chlorite ($d_{001} \sim 14$ Å) and variable combinations of these minerals, with random stacking of the different (001) layers down to the unit-cell scale ("mixed layers"). The TEM is a useful analytical tool for studying clay minerals, because they have a grain size smaller than 2 μm and often form ultrathin lamellae a few lattice fringes thick. Moreover, clays are typically affected by (001) layer bending, delamination, interlayer partings and partial amorphization. For these reasons, several studies on clay-bearing faults have been recently supported by TEM data (e.g., Yan et al., 2001; Solum et al., 2003, 2005; Schleicher et al., 2006, 2011; Boutareaud et al., 2010). Clays have been detected in the Punchbowl fault core, where undeformed ordered polytypes of chlorite/muscovite evolve to "hairy" disordered chlorite/smectite (Solum et al., 2003). Clays have been detected by TEM in the Moab fault gouge (Solum et al., 2005) and in the San Andreas fault (e.g., Schleicher et al., 2006, 2010; Van der Pluijm et al., 2010). Schleicher et al. (2006) described the occurrence of wavy Ca-K-bearing smectitic lamellae, down to a few nanometer thick, formed by nucleation and growth during fault creep and favoured by low-T aqueous fluid circulation along shallow portion of the San Andreas fault. Recent TEM studies also determined detailed nanostructure for so-called clay clast aggregates (CCA), found in fault gouges from shallow seismogenic faults and in rotary shear experimental samples (Boutareaud et al., 2010). The authors describe the complex concentric structure of the CCA, observing (from inner to outer shells): I) the clast (50 μm, average value), II) a micrometer thick cataclastic porous layer, III) a 20–50 nm thick layer of clays, with strong preferred orientation parallel to clast margin, and IV) a cortex composed essentially of illite-smectite mixed layers (evolving from preferred to random orientations).

Fault rocks may also contain amorphous phases (e.g., Wenk, 1978; Warr et al., 2003; Di Toro et al., 2004; Ozawa and Takizawa, 2007; Janssen et al., 2010), which have been interpreted to result from a) extreme comminution with complete loss of long-range structural order, at relatively low P/T conditions; b) decomposition and amorphization reactions, at variable P/T conditions; and c) rapid quench from a melted phase. The occurrence and the spatial distribution of an amorphous material can be easily checked by SAED and corresponding images. As previously stated, amorphous phases do not produce diffraction spots (e.g., SAED pattern in Fig. 1f), and give rise to "flat", contrast-free images, without traces of lattice fringes even at very high magnification. Furthermore, unbiased EDS compositions and the identification of possible crystalline inclusions, that can be either crystalline relicts from the host rock or newly formed crystallites, provide the evidence for understanding amorphous formation. Accurate EDS chemical data are obtained by focussing the electron beam on the amorphous matrix with a spot size of a few nm, avoiding interference from possible inclusions. For submicrometric crystalline inclusions, the TEM provides accurate determinations of crystal structure, deformation-induced defects, chemical composition, size and shape (e.g., euhedral versus anhedral, lobate boundaries, etc.), allowing relict clasts to be distinguished from neoformed grains. A straightforward example is given by Warr et al. (2003), who investigated a symmetrically layered pseudotachylyte vein from the Alpine Fault, New Zealand. TEM results, summarized in their Fig. 3, unequivocally documented the occurrence of partially decomposed biotite relicts, surrounded by a silica-rich glass that was produced by frictional melting during seismic slip. Based on biotite deformation nanostructures and polytypic characteristics, the authors distinguished a second generation of biotite that overgrew previous biotite grains. The TEM observations allowed a detailed reconstruction of the pseudotachylyte history, pointing to cyclic pulses of heating, melting and crystallization. Other examples of TEM studies reporting the occurrence of amorphous phases in natural fault rocks, as pseudotachylytes and also experimentally deformed samples, are Weiss and Wenk (1983), Macaudiere et al. (1985), Yund et al. (1990), Magloughlin (1992), Goodwin (1999), Warr et al. (2003), Otsuki and Monzawa (2003), Moecher and Brearley (2004), Ozawa and Takizawa (2007), Ujiie et al. (2007), Janssen et al. (2010), Viganò et al. (2011).

3.3. Nanoscale investigation of deformation-induced mineral reactions

Identification of mineral reactions, which occur during or after formation of a fault rock requires the accurate mineralogical identification of reactants and products, and the definition of their microstructural relationships. While these features can be characterized by conventional petrographic or SEM investigations for most rocks, TEM is needed in ultrafine-grained and poorly crystalline fault rocks. The correct identification of mineral reactions and resulting mineral assemblages enhances fault understanding. In many cases, deformation-induced reactions within the brittle crust result in significant mechanical weakening, predominantly through hydration reactions forming weak minerals (e.g., Wintsch et al., 1995). However, changes in local physico-chemical conditions can also trigger the formation of stronger assemblages (e.g. Wibberley, 1999). Additionally, mineral reactions involving dehydration and decarbonation produce substantial fluid release within the fault zone, of H_2O and CO_2, respectively, also influencing fault mechanical behaviour. Lastly, the correct identification of a mineral reaction may reliably estimate the P/T conditions of faulting. The

following examples focus on decarbonation and dehydration processes at different P/T and dynamic conditions, from the huge array of deformation-induced mineral reactions that can occur within fault rocks.

3.3.1. Dolomite decarbonation reactions

Dolostone-hosted fault zones are often characterized by the occurrence of talc, formed by interaction of dolomite with silica-rich fluids at relatively low temperature (250–400 °C at 1–2 kbar), according to the reaction $3MgCa(CO_3)_2 + 4SiO_2 + H_2O = Mg_3Si_4O_{10}(OH)_2 + 3CaCO_3 + 3CO_2$ (Viti and Collettini, 2009, and reference therein). Fig. 3a and b show representative TEM images of faulted dolostone, characterized by the close association of dolomite (dol) and calcite (cal) crystals, from an example along the Zuccale low-angle normal fault outcropping in Elba Island, Italy (Viti and Collettini, 2009). Whereas dolomite exhibits strain contrast features indicative of defective and strained crystal structure, associated calcite always shows a homogeneous TEM contrast, suggesting undeformed, defect-free structure. This was interpreted to indicate that dolomite deformation predates calcite precipitation. The involvement of silica-rich fluids in the above reaction has been also confirmed at the TEM scale, where nanometer-sized veins of poorly crystalline silica and randomly oriented quartz are intermixed with carbonate grains (e.g., Fig. 3c). Incipient talc crystallization occurs at carbonate grain boundaries (Fig. 3d), where talc lamellae a few nanometers thick are commonly associated with poorly crystalline material. The progressive, deformation-assisted replacement of dolomite results in well foliated talc-bearing horizons, consisting of preferentially oriented talc (001) lamellae, up to 200–300 nm thick (Fig. 3e and f). The extent of talc preferred orientation can be easily checked by SAED patterns (insets in Fig. 3e and f), measuring the angular divergence among c* reciprocal axes, where higher divergence means greater variability in orientation of talc crystals.

At different geodynamical and chemical conditions, dolostones may breakdown to Mg-rich calcite + periclase (MgO) + CO_2 (at ~550 °C). This reaction can be triggered by frictional heating during seismic slip, as demonstrated by De Paola et al. (2011), who investigated the slipping surface (<100 μm thick) of a dolomite sample deformed in a high velocity rotary apparatus ($v > 1$ m/s and displacement larger than 1 m). The TEM study revealed that dolomite break-down produces an ultrafine assemblage of randomly oriented, defect-free crystalline grains, up to 20 nm in size, with ill-defined crystal boundaries locally evolving to polygonal-like textures (Fig. 4a and b). Lattice spacings determination from single-crystal and polycrystalline ring-shaped SAED patterns (e.g., inset in Fig. 4a), coupled with focused EDS data, allowed the accurate identification of relict dolomite and neo-formed Mg-rich calcite. These data also demonstrated a progressive increase in d_{hkl} distances with increasing Ca/Mg ratio in the carbonate (e.g., measured d_{104} from 2.86 Å in relic dolomite clasts to 3.00 Å in Mg-rich calcite nanograins).

These two examples point out that, depending on P/T and stress conditions, and on the nature of circulating fluids, dolomite decarbonation may result in completely different fault rocks, with different mechanical behaviour. In the first example, the pervasive, low-temperature crystallization of weak talc causes a significant reduction of the fault friction coefficient, leading to a dominant deformation mechanism of mineral weakening. In the second example, the decomposition of dolomite by frictional heating causes, on one side, a significant release of CO_2, and, on the other side, the formation of an ultrafine grained assemblage, both assisting fault weakening by thermal pressurization and powder lubrication mechanisms (Rice, 2006 and Han et al., 2011, respectively).

3.3.2. Serpentine dehydration reactions

Serpentinitic rocks consist predominantly of poorly crystalline assemblages of fine/ultrafine lizardite, antigorite and chrysotile (i.e., they are typical subjects for TEM investigation), and are believed to play a chief role in lithosphere dynamics (e.g., Reinen et al., 1991). Where serpentinites are affected by faulting, the overall picture is complicated by deformation and enhanced reactivity, commonly resulting in dehydration processes. To understand the potential implications of these reactions, serpentine dehydration is thought to play a main role in the temperature-dependent transition from ductile to brittle (dehydration embrittlement; Raleigh and Paterson, 1965), and in the distribution of intermediate-depth seismicity (Peacock, 2001; Dobson et al., 2002; Jung and Green, 2004). Depending on P/T conditions, serpentine dehydration may give rise to weak talc and/or to strong amphibole, olivine and pyroxene, in a range of extremely different micro/nanostructures. This behaviour implies that the resulting fault rocks may exhibit contrasting mechanical behaviours, requiring correct identification of serpentine reaction products and corresponding micro/nanostructural arrangement to provide accurate evaluations.

Evidence of serpentine dehydration has been observed in experimentally deformed lizardite + chrysotile serpentinites (torsion experiments at 550–650 °C and 300–400 MPa; Hirose et al., 2006; Viti and Hirose, 2009). Fig. 5a shows a representative TEM image of the reaction front of lizardite (left upper corner, dark

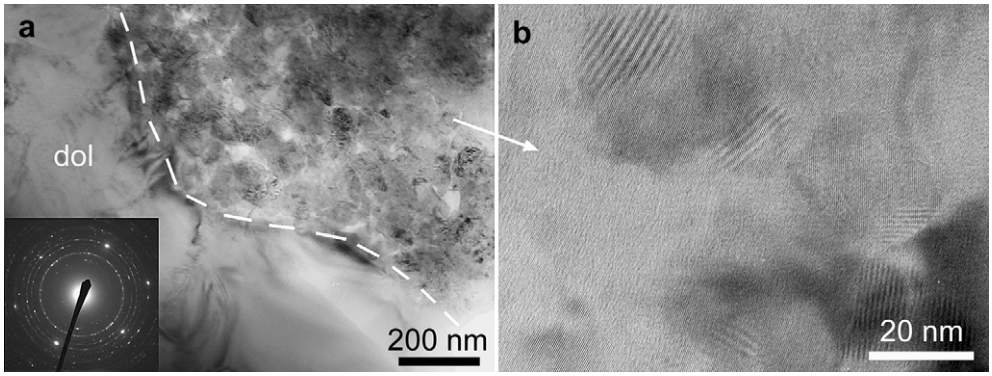

Fig. 4. (a) Dolomite reaction front (dashed line) in experimentally deformed sample from a high-velocity rotary experiment. Dolomite decomposition product (upper right corner) consists of ultrafine nanocrystals in random orientation as indicated by the inset ring-shaped SAED pattern. (b) HRTEM detail of defect-free nanocrystals of Mg-rich calcite in variable orientation, as testified by the variable spacings of lattice fringes. The broader "lines" are interference effects ("moiré" fringes) between ultra-thin overlapping crystals.

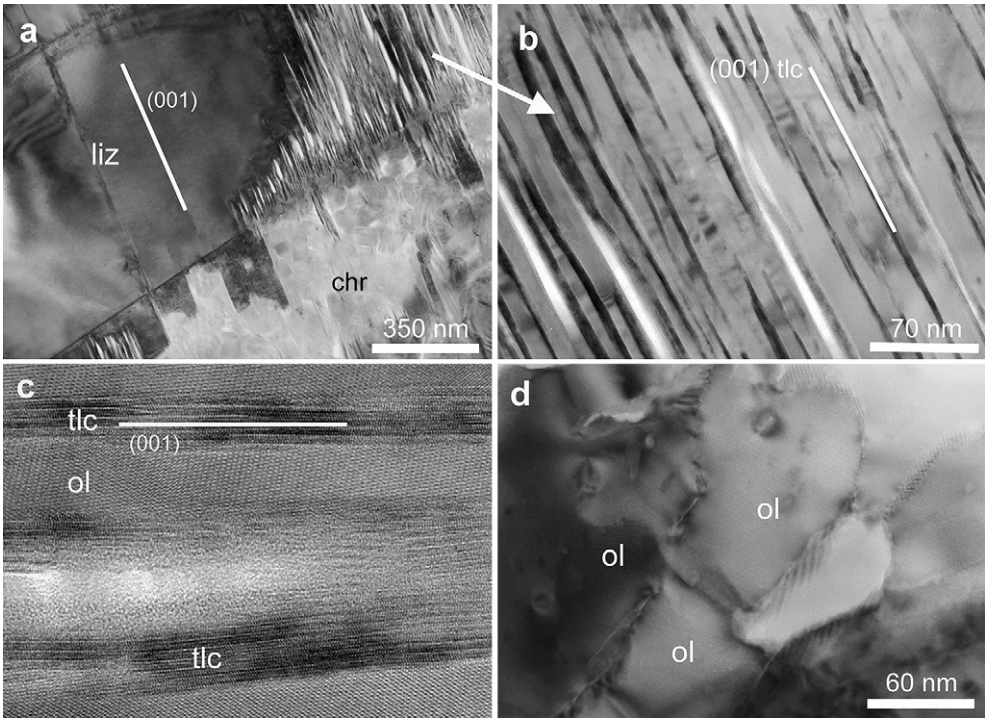

Fig. 5. TEM images relative to serpentine breakdown reaction in experimentally deformed serpentinites (modified from Viti and Hirose, 2009). Orientations of (001) planes shown in a-c. (a) Lizardite crystal (liz; upper left corner) and associated chrysotile matrix (chr; lower right corner). Lizardite is partially replaced by a lamellar and porous material (upper right corner). (b) Detail of the lizardite decomposition product, consisting of a nanometer-sized association of (001) talc lamellae (dark) and forsteritic olivine (light). (c) High-resolution detail of the ultrafine association of talc (001) lamellae (9 Å-spaced) and olivine (ol) crystals. (d) Representative image of chrysotile decomposition product, mostly consisting of healed olivine grains. The variable TEM contrast of nearby olivine grains is due to different crystal orientations.

contrast), replaced by an ultrafine lamellar intergrowth of olivine crystals (up to 50 nm thick) and (001) talc lamellae (up to 20–30 nm thick), parallel to (001) lizardite (Fig. 5b). Fig. 5c shows a high-resolution detail of lizardite decomposition products, with ultrafine talc lamellae (tlc; a few unit-cell thick), interlayered with crystalline, defect-free olivine (ol). Associated chrysotile also underwent dehydration, giving rise to a different anhydrous nanotexture, with predominant, closely associated forsterite grains (Fig. 5d).

As with dolomite decarbonation, serpentine dehydration can be triggered by frictional heating during seismic slip (e.g., Hirose and Bystricky, 2007). For example, Viti and Hirose (2010) investigated the 200 μm-thick slip zone produced by high-velocity deformation of antigorite, revealing an asymmetric thermal gradient from the host undeformed rock towards the slipping surface. At the host rock/slip zone boundary, antigorite crystals underwent partial dehydration and decomposition (Fig. 6a and b). Fig. 6a shows the reaction front of antigorite, broadly parallel to $(001)_{atg}$ cleavage planes (white line). The NE-trending lattice fringes correspond to antigorite TO layer corrugation, with average superperiodicity of ~40 Å. Antigorite lamellae are progressively replaced by a porous, "sponge-like" material (Fig. 6a and b; arrows point to large elongated pores). SAED diffraction patterns (always weak, diffuse and ring-shaped) and TEM/EDS analyses indicate that the decomposition product is amorphous to poorly crystalline, with bulk anhydrous composition close to that of the antigorite. Toward the slip surface, the antigorite dehydration product transforms to an unexpected material with high crystallinity, grain size of 100–200 nm, low porosity and sharp grain boundaries, recalling typical annealing structures (Fig. 6c). SAED patterns (Fig. 6d) and TEM/EDS analyses performed on single nanograins, allowed the accurate identification of the newly formed crystals, revealing forsterite and enstatite (average atoms per formula units, a.p.f.u., $Mg_{1.95}$ $Fe_{0.06}$ $Si_{0.99}$ and $Mg_{1.71}$ $Fe_{0.10}$ $Al_{0.09}$ $Si_{2.05}$, on the basis of 4 and 6 oxygens, respectively). Forsterite and enstatite are randomly intermixed, but they can be distinguished in TEM images because of the slightly larger size of forsterite grains and the typical lamellar contrast of enstatite grains due to polytypic disorder (arrow in Fig. 6c). The behaviour of compact ultrafine assemblages, like those shown in Figs. 2a, 5d and 6c, is not completely clear. As remarked by Brodie and Rutter (1987), the small grain size leads to mechanical weakening through diffusion and plasticity-accommodated grain-boundary sliding. However, weakening could be only a transient condition, because prograde metamorphism may promote grain coarsening and healing processes, leading to progressive hardening.

3.4. Typical deformation-induced nanostructures in phyllosilicates

The TEM has been largely used to study the intracrystalline deformation structures in rock-forming minerals such as carbonates, feldspars, quartz and olivine (e.g., Barber and Wenk, 1976; Tullis and Yund, 1980; McLaren, 1991; Green, 1992; Kennedy and White, 2001), with major attention to dislocations, twins and subgrain boundaries, although usually in dark-field imaging mode. In phyllosilicates, deformation mechanisms result from a complex interplay among 1) the extent of crystal preferred orientation; 2) the nature and the strength of interlayer bonds; and 3) the conditions of deformation and faulting. Deformation mechanisms in phyllosilicates are strongly controlled by their layered structure and by their typically weak interlayer bonds, commonly resulting in (001) interlayer delamination and parting, (001) stacking faults and polytypic disorder. The relatively low energy required to activate these processes implies that almost all deformed phyllosilicates

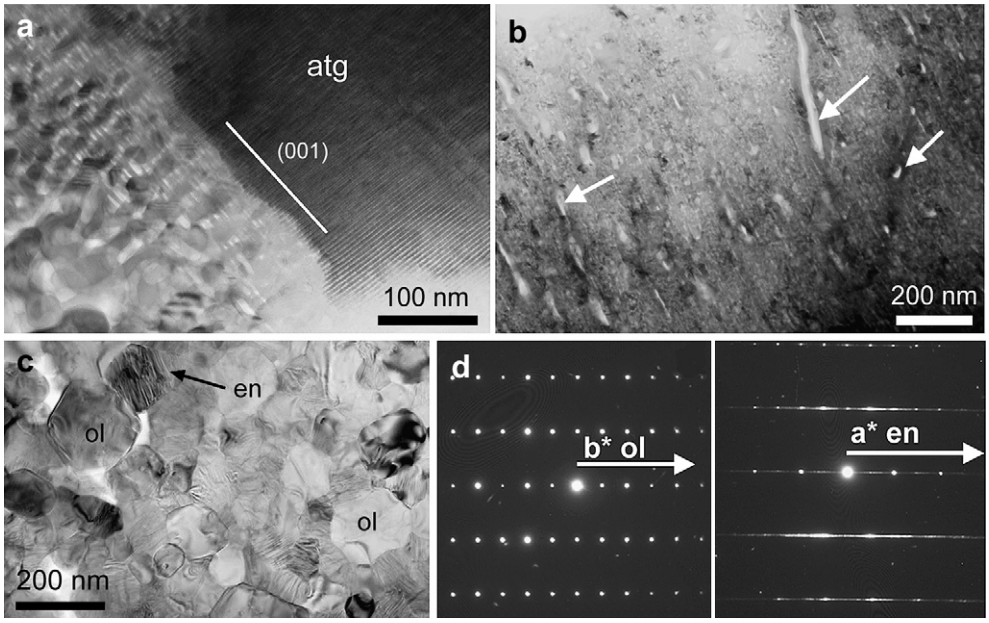

Fig. 6. TEM images for serpentine breakdown by frictional heating in experimentally deformed serpentinites (modified from Viti and Hirose, 2010). (a) Antigorite (atg) reaction front, with highly porous, poorly crystalline reaction product (lower left corner, light contrast). (b) Detail of the antigorite dehydration/decomposition product. Pores (arrows) are commonly merged into larger elongate pore spaces. (c) High-crystallinity assemblage occurring at the slipping surface and consisting of forsteritic olivine (ol) and enstatite (en), with typical polygonal-like grain boundaries. Enstatite crystals always show lamellar TEM contrast (arrow) due to polytypic disorder. (d) SAED patterns from an olivine single crystal (left side; b*c* orientation, with sharp and intense reflections) and from an enstatite single-crystal (right side; a*c* orientation, with intense a* streaking due to polytypic disorder).

exhibit these deformation-induced nanostructures. Interlayer delamination can be the dominant deformation mechanisms in weak phyllosilicates like clays and talc, which are therefore good candidates for strain accommodation through enhanced frictional slipping parallel to (001). Different deformation mechanisms may occur in relatively strong phyllosilicates, where intracrystalline folding, kinking and cataclasis have been often documented. These kinds of nanostructures preferentially occur in deformed phyllosilicates from metamorphic rocks rather than from brittle faults, suggesting that they are favoured during increasing P/T conditions. Amouric (1987) and Merriman et al. (1995) described TEM-scale kinks and chevron-type folds in metamorphic chlorites. Kinks in natural and experimentally deformed micas are described by Bell et al. (1986), who reported an extensive TEM investigation of kinking behaviour, focussing on the role of dislocations and cleavage. Goodwin and Wenk (1990) documented the occurrence of intracrystalline folding, looping and cataclasis in natural biotite. Similar features have been also observed in muscovites (e.g., Ahn et al., 1985).

TEM-scale kinking has been documented in experimentally deformed talc at relatively high pressures and temperatures (Escartin et al., 2008). The authors observed that talc deformation was accommodated by a combination of crystal plasticity, frictional sliding and cataclasis at all temperatures up to dehydration, and that kinking was favoured for increasing temperature.

The occurrence of kinks in experimentally deformed serpentine was documented by Viti and Hirose (2009). Fig. 7a shows a TEM image of an experimentally deformed lizardite affected by intense kinking. Kink axial planes occur at a high angle with respect to (001) and represent sites of preferential strain accumulation and enhanced reactivity. Kink axial planes are not parallel and they give rise to interpenetrating lizardite sectors, analogous to conjugate fault systems (Fig. 7a). Fig. 7b shows a detail of kinked lizardite, with evident change in (001) lattice fringe orientation across the kink axial plane. The planar arrangement of (001) layers in lizardite and the occurrence of relatively strong interlayer bonds probably play a role in serpentine deformation mechanisms. In fact, at the same experimental conditions, chrysotile (i.e., the serpentine variety with rolled (001) layers and weaker interlayer bonds; Fig. 7c) does not exhibit kinks, but rather a peculiar squeezing mechanism, associated with intense (001) delamination, dramatic loss of cohesion across the layers and partial amorphization (Fig. 7d).

Interlayer delamination is almost ubiquitous in deformed phyllosilicates, and is typically associated with (001) slip (e.g., Banos et al., 1983; Goodwin and Wenk, 1990; Escartin et al., 2008; Viti and Collettini, 2009). The extent of interlayer delamination significantly increases in those phyllosilicates where the interlayer bond is particularly weak, as in talc and smectite (e.g., Morrow et al., 2000). In these cases, pervasive interlayer delamination may result in a further decrease of friction coefficient, and in enhanced mineral weakening processes. Fig. 7e shows the typical deformation-induced nanotexture of talc within the Zuccale fault core. Talc lamellae (originally 200–300 nm thick) are pervasively delaminated, with fissuring and partial amorphization along the interlayer surfaces (Fig. 7f). Nanoscale delamination induces a one-order magnitude grain size reduction from 200–300 to 10–20 nm, enhancing the slip processes. A similar process has been described by Bell and Wilson (1981), who documented grain size reduction in biotite through “segmentation” parallel to (001) planes.

Deformation of layer silicates may also induce stacking faults, i.e. “mistakes” in the overlapping sequence of (001) planes (e.g., Bell and Wilson, 1981; Bons and Schryvers, 1989; Goodwin, 1995; Banfield et al., 1995; Viti and Hirose, 2009; Viti and Collettini, 2009). The occurrence of stacking faults can be easily verified in SAED patterns, because they produce evident streaking in the c* direction (e.g., Fig. 7e, inset). Stacking “mistakes” can be due to intercalations of different phyllosilicates (e.g., a layer of chlorite within a serpentine crystal, producing a TEM image with a single broad 14 Å lattice fringe within a regular sequence of 7 Å-spaced lattice fringes), but in several cases they are due to variable stacking

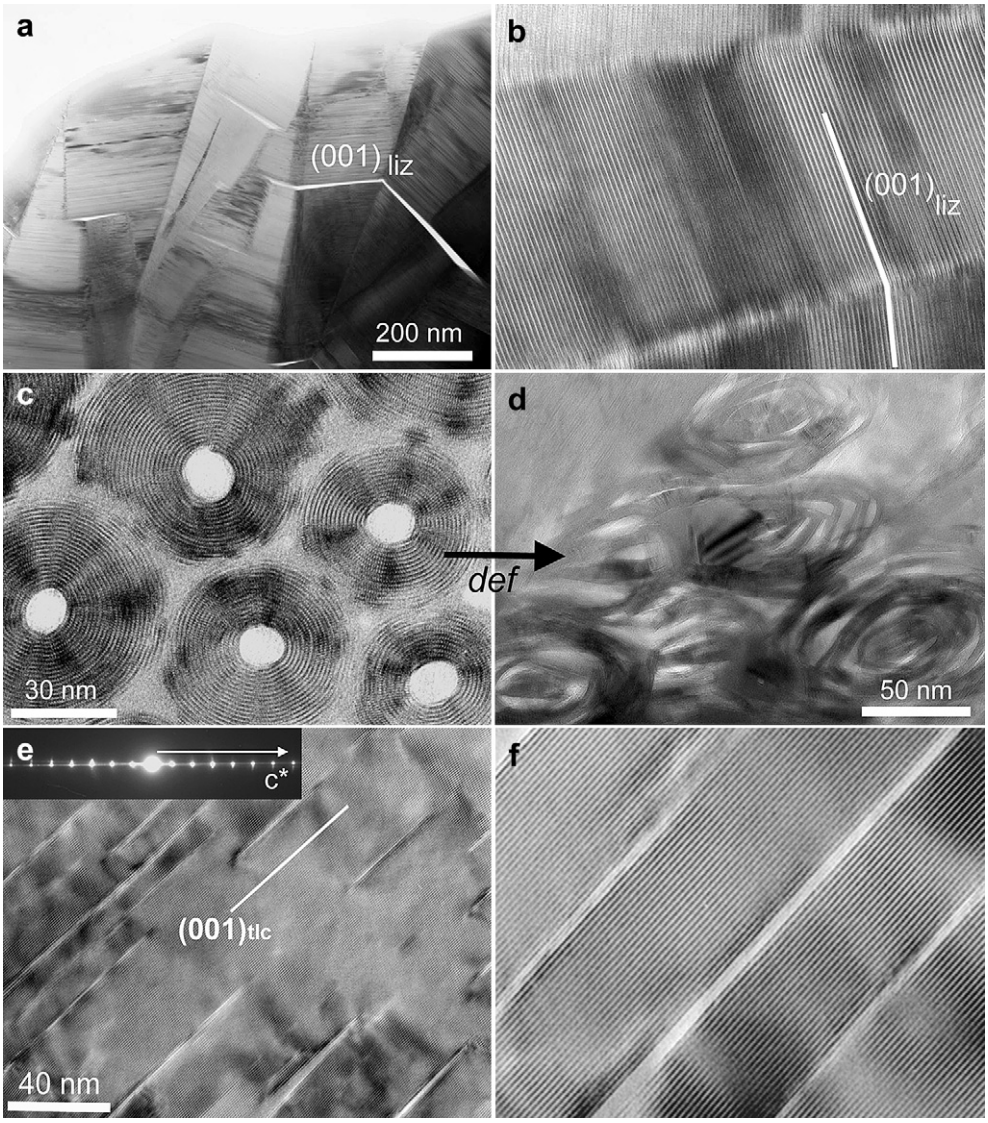

Fig. 7. (a) Intense kinks in experimentally deformed lizardite through high-T torsion deformation experiments (Viti and Hirose, 2009). Planar white features correspond to lizardite (001) interlayer fissuring, pointing out the sharp change in $(001)_{liz}$ orientation across kink axial planes. (b) Detail of two nearby kink axial planes in deformed lizardite, showing the sharp changes in the 7 Å-spaced (001) lattice fringes. (c) Representative TEM image of closely packed undeformed chrysotile fibres with perfectly circular cross-sections. 7 Å-spaced lattice fringes are completely rolled around the central hole (white central portions). (d) Experimentally deformed chrysotile fibres, characterized by elliptical cross-sections and broad interlayer fissuring. (e) Interlayer delamination in talc from the Zuccale fault and corresponding SAED pattern, showing intense c* streaking due to polytypic disorder (inset). Lattice fringes are approximately 9 Å-spaced and correspond to talc (001) layers. (f) Detail of talc (001) delamination, resulting in 10–30 nm thick "sub-lamellae", separated by poorly crystalline to amorphous material (modified from Viti and Collettini, 2009).

of the same layer (i.e., polytypic disorder). Still, not all stacking faults in layer silicates are related to deformation. In particular, polytypic disorder may represent a growth feature predating deformation, whereas the intercalation of low-temperature phyllosilicates may be due to post-deformation weathering effects (e.g., Bons and Schryvers, 1989). TEM observations are therefore necessary to understand the nature of stacking mistakes and their actual relationships with deformation. Banfield et al. (1995) investigated the relationships between deformation and stacking sequences in serpentine minerals. The authors documented the occurrence of a strong lineation in the foliation, due to preferred orientation of a and b axes of serpentine parallel to shear direction. Lineation would have formed by crystallographically controlled, syn-dynamic rotations of serpentine layers and/or by recrystallization processes. Deformation-induced polytypic mistakes were observed in experimentally deformed serpentine (Viti and Hirose, 2009) and natural talc (Viti and Collettini, 2009). In both cases, deformation determined completely disordered polytypes, with a random sequence of left-slanting, right-slanting and orthogonal stacking vectors (e.g., Fig. 2d, deformed lizardite). These findings are in agreement with Goodwin and Wenk (1990), who documented the evolution of the stacking sequence of biotite with increasing deformation. The authors observed that periodic stacking faults produced a four-layers ordered superstructure, generating sharp extra reflections in corresponding SAED patterns. However, with increasing deformation, the ordered superstructure is replaced by a completely disordered stacking sequence, as testified by c* streaking and concomitant decrease in the extra reflection intensity.

4. Discussion and conclusions

Previous sections aimed to demonstrate the potentials of TEM investigation in fault-rock studies, giving special emphasis to the

accurate characterization of ultrafine-grained polymineralic assemblages, poorly crystalline minerals, amorphous phases, deformation-induced nanostructures and mineral reactions.

The fine/ultrafine fraction has a fundamental role in fault slip mechanisms, in the earthquake energy budget and in fault rock reactivity (e.g., Brodie and Rutter, 1987; Wilson et al., 2005; Carpinteri and Paggi, 2005; Chester et al., 2005; Liu and Cao, 2006; Sammis and Ben-Zion, 2008; Han et al., 2010, 2011). Wilson et al. (2005) proposed that ultrafine-grained gouges, formed by dynamic pulverization during seismic slip, control earthquake instabilities, and focussed on the role of the gouge surface energy in the earthquake energy budget. A quantitative evaluation of the fracture surface energy demonstrated that the fracture surface energy is dependent on grain size and, particularly, on the surface area of nanosized particles occurring in the ultracataclasite (Chester et al., 2005).

The occurrence of ultrafine grained particles is thought to play a role in slip weakening mechanisms, as reported by Han et al. (2010), for which ultrafine particles may lubricate faults quite effectively at seismic slip rates (powder lubrication). Similarly, Carpinteri and Paggi (2005) explain the apparent weakness of the San Andreas fault as a consequence of size-scale effects on the friction coefficient. Sammis and Ben-Zion (2008) claimed that particles smaller than a specific size limit are observed to deform plastically, changing their shape rather than fragmenting via fracturing, and that the observation of nanosized fragments in a fault rock also limits the amplitude and the duration of the thermal pulse generated during seismic movement, because of grain growth kinetics. The same authors, recalling the study by Chester et al. (2005), suggested that the observation of 4 nm particles implies that temperatures could not have reached 800 °C. However, this conclusion is strongly dependent on the nature of nanosized particles. In fact, if the nanoparticles were precipitated or crystallized from a glass, they cannot be used to constrain the amplitude and duration of thermal pulses, further necessitating TEM investigations.

The importance of nanoscale investigations in mechanical studies is also emphasized by the recent development of new disciplines such as nanotribology and nanomechanics (e.g., Bhushan, 2005; Carpinteri and Paggi, 2005; Mo et al., 2009). These disciplines investigate the mechanical and frictional properties of nanostructured materials, pointing out that nanostructured materials have completely different behaviour with respect to the equivalent coarser counterparts. The influence of grain characteristics such as size, particle size distribution, shape or roughness on the frictional properties of fault gouges was investigated by Mair et al. (2002), who considered grain sizes of 0.5–0.6 μm. Similar investigations (with TEM observations) for grain sizes that are one-order of magnitude smaller, have been recently done by Han et al. (2011). They performed friction experiments on periclase nanoparticles at seismic rates, finding significant decrease in dynamic friction coefficient and confirming that the formation of nanoparticles in slip zones may be an important fault lubrication process.

The examples reported in this paper also demonstrate that the TEM can be indispensable for the (typically not straightforward) identification of poorly crystalline, fine-grained minerals, like clays and talc. The main implication in structural geology studies is that clays, particularly smectite, and talc are among the weakest materials in geological samples with friction coefficients as low as ~0.05–0.2, and are thought to significantly influence fault frictional properties, causing weakening and aseismic slip (e.g., Morrow et al., 2000; Saffer and Marone, 2003; Moore and Lockner, 2004, 2008; Moore and Rymer, 2007; Wibberley, 2007; Collettini et al., 2009a; Schleicher et al., 2011). The weak mineral nanostructure, including size, preferred orientation, development of interconnected or discontinuous foliation, deformation defects, extent of delamination, is also of primary interest. It is commonly assumed that fault cores must be clay- or talc-dominated to effectively affect fault strength and explain fault weakness. However, fault rocks with relatively small contents in weak minerals may be weak, due to micro/nanostructural effects and, specifically, to the formation of interconnected continuous weak films (e.g., Collettini et al., 2009a, b; Schleicher et al., 2011). In the Zuccale samples, the occurrence of interconnected talc horizons and of pervasive deformation-induced delamination results in a nearly infinite number of sliding surfaces and in extremely low friction coefficient (Collettini et al., 2009b). Schleicher et al. (2011) reported the occurrence of pervasive interconnected clay-bearing nanocoatings in fault rock samples from the San Andreas fault and remarked their role in fault weakening and creep behaviour. Fault weakness has been also related to the occurrence of serpentine (e.g., Reinen et al., 1991; Escartin et al., 2001), even though friction experiments have demonstrated that the different serpentine varieties have significantly different friction coefficients (e.g., Reinen et al., 1994; Moore et al., 1996, 1997). Consequently, only chrysotile can be strictly considered as a weak mineral. As previously stated, an accurate distinction between weak chrysotile and strong lizardite/antigorite within deformed serpentinites requires the use of TEM.

TEM can be necessary for the correct identification of deformation-induced mineral reactions as well as for the detection and characterization of possible amorphous phases. Cyclic oscillations in the physico-chemical conditions, both in time and space, may trigger mineralogical and structural changes at the sub-micron scale, that obviously affect the mechanical properties of the fault rock. For example, weak minerals like clays, talc or chrysotile may evolve to stronger assemblages under increasing metamorphic conditions, but subsequent retrograde metamorphism may reverse the reaction, leading to the precipitation of weak phases (and vice versa). The knowledge of reactants, products (either crystalline or amorphous) and of their nanostructural relationships allows, on one hand, discrimination among multiple genetic mechanisms. For example, does a pseudotachylite sample have a melt origin or does it derive from ultracomminution processes? On the other hand, the identification of the mineral reaction may provide useful constraints about the physical and chemical conditions during faulting. For example, Moecher and Brearley (2004) observed euhedral crystals of mullite and magnetite within a natural pseudotachylite and interpreted them as the devitrification products of an originally molten phase, implying that frictional heating reached a temperature of 1150–1200 °C. The examples of dolomite decarbonation and serpentine dehydration induced by frictional heating also allow confident temperature estimations. In particular, the observed high-T assemblages (Mg-rich calcite + periclase and forsterite + enstatite) indicate that frictional heating peaked higher than 550 °C and 820 °C in dolostone and serpentinite, respectively. Similarly, based on TEM observations of a carbonate pseudotachylyte, Viganò et al. (2011) suggested the formation of a melt approximately at $T = 700$ °C and $P = 0.1$–0.2 GP, followed by rapid crystallization.

Summarizing, the examples addressed here have highlighted the advantages of a multidisciplinary approach, showing that several fundamental features of fault rocks occur at a submicrometric scale. These submicrometric features can be accurately determined only by combining images with diffraction and chemical data at a nanoscale resolution. This nanoscale inspection does and will significantly contribute to our understanding of fault mechanical behaviour and faulting conditions.

Acknowledgements

Most of the observations reported in this review derive from scientific collaborations with Cristiano Collettini (University of

Perugia, Italy), that is acknowledged for its fundamental scientific support, Takehiro Hirose (Kochi, Japan) and Nicola De Paola (Durham University). L. Goodwin is acknowledged for her excellent review and helpful suggestions.

References

Ahn, J.H., Peacor, D.R., Essene, E.J., 1985. Coexisting paragonite-phengite in blueschist eclogite: a TEM study. American Mineralogist 70, 1193–1204.

Andreani, M., Boullier, A.M., Gratier, J.P., 2005. Development of schistosity by dissolution-crystallization in a Californian serpentinite gouge. Journal of Structural Geology 27, 2256–2267.

Amouric, M., 1987. Growth and deformation defects in phyllosilicates as seen by HRTEM. Acta Crystallographica B43, 57–63.

Banfield, J.F., Bailey, S.W., Barker, W.W., Smith, R.C., 1995. Complex polytypism: relationships between serpentine structural characteristics and deformation. American Mineralogist 80, 1116–1131.

Banos, J.O., Amouric, M., De Fouquet, C., Baronnet, A., 1983. Interlayering and interlayer slip in biotite as seen by HRTEM. American Mineralogist 68, 754–758.

Barber, D.J., Wenk, H.-R., 1976. Transmission Electron Microscopy of Experimentally and Naturally Deformed Carbonates.

Bell, I.A., Wilson, C.J.L., 1981. Deformation of biotite and muscovite: TEM microstructrure and deformation model. Tectonophysics 78, 201–228.

Bell, I.A., Wilson, C.J.L., McLaren, A.C., Etheridge, M.A., 1986. Kinks in mica: role of dislocations and (001) cleavage. Tectonophysics 127, 49–65.

Bhushan, B., 2005. Nanotribology and nanomechanics. Wear 259, 1507–1531.

Bons, A.J., Schryvers, D., 1989. High-resolution electron microscopy of stacking irregularities in chlorites from the central Pyrenees. American Mineralogist 74, 1113–1123.

Boutareaud, S., Boullier, A.M., Andreani, M., Calugaru, D.G., Beck, P., Song, S.R., Shimamoto, T., 2010. Clay clast aggregates in gouges: new textural evidence for seismic faulting. Journal of Geophysical Research 115, B02408.

Brodie, K.H., Rutter, E.H., 1987. The role of transiently fine-grained reaction products in syntectonic metamorphism: natural and experimental examples. Canadian Journal of Earth Science 24, 556–564.

Buseck, P.R., 1992. Minerals and Reactions at the Atomic Scale: Transmission Electron Microscopy. In: Reviews in Mineralogy, vol. 27. Mineralogical Society of America, Washington DC.

Carpinteri, A., Paggi, M., 2005. Size-scale effects on the friction coefficient. International Journal of Solids and Structures 42, 2901–2910.

Chester, J.S., Chester, F.M., Kronenberg, A.K., 2005. Fracture surface energy of the Punchbowl fault, San Andreas system. Nature 437, 133–136.

Chipera, S.J., Bish, D.L., 2002. FULLPAT: a full-pattern quantitative analysis program for X-ray powder diffraction using measured and calculated patterns. Journal of Applied Crystallography 35, 744–749.

Christie, J.M., Ardell, A.J., 1976. In: Wenk (Ed.), Deformation Structures in Minerals. Springer-Verlag, Berlin Heidelberg New York, pp. 374–403.

Collettini, C., Viti, C., Smith, S.A.F., Holdsworth, R.E., 2009a. The development of interconnected talc networks and weakening of continental low-angle normal faults. Geology 37, 567–570.

Collettini, C., Niemeijer, A., Viti, C., Marone, C., 2009b. Fault zone fabric and fault weakness. Nature 462, 907–911.

De Paola, N., Hirose, T., Mitchell, T., Di Toro, G., Viti, C., Shimamoto, T., 2011. Fault lubrication and earthquake propagation in thermally unstable rocks. Geology 39, 35–38.

Dewers, T., Wilson, B., Reches, Z., 2003. Scaling Particle Size in Fault Gouge: Variable Fractal Dimension or Non-Fractal Distribution? AGU Fall Meeting abstract, #NG12C-06.

Di Toro, G., Goldsby, D.L., Tullis, T.E., 2004. Friction falls towards zero in quartz rock as slip velocity approaches seismic rates. Nature 427, 436–439.

Dobson, D.P., Meredith, P.G., Boon, S.A., 2002. Simulation of subduction zone seismicity by dehydration of serpentine. Science 298, 1407–1410.

Escartin, J., Hirth, G., Evans, B., 2001. Strengths of slightly serpentinized peridotites: implications for the tectonics of oceanic lithosphere. Geology 29, 1023–1026.

Escartin, J., Andreani, M., Hirth, G., Evans, B., 2008. Relationships between the microstructural evolution and the rheology of talc at elevated pressures and temperatures. Earth and Planetary Science Letters 268, 463–475.

Goodwin, L.B., Wenk, H.-R., 1990. Intracrystalline folding and cataclasis in biotite of the Santa Rosa mylonite zone: HVEM and TEM observations. Tectonophysics 172, 201–214.

Goodwin, L.B., 1995. Development of phyllonite from granodiorite: mechanisms of grain-size reduction in the Santa Rosa mylonite zone, California. Journal of Structural Geology 17, 689.

Goodwin, L.B., 1999. Controls on pseudotachylyte formation during tectonic exhumation in the south mountains metamorphic core complex, Arizona. In: Ring, U., Brandom, M.T., Lister, G.S., Willet, S.D. (Eds.), Geological Society, London Special Publications, vol. 154, pp. 325–342.

Green, H.W., 1992. Analysis of deformation in geological materials. In: Buseck (Ed.), Reviews in Mineralogy, vol. 27, pp. 425–454.

Han, R., Hirose, T., Shimamoto, T., 2010. Strong velocity weakening and powder lubrication of simulated carbonate faults at seismic slip rates. Journal of Geophysical Research 115, B03412.

Han, R., Hirose, T., Shimamoto, T., Lee, Y., Ando, J., 2011. Granular nanoparticles lubricate faults during seismic slip. Geology 39, 599–602.

Hirose, T., Bystricky, M., Kunze, K., Stuniz, H., 2006. Semi-brittle flow during dehydration of lizardite-chrysotile serpentinite deformed in torsion: implications for the rheology of oceanic lithosphere. Earth and Planetary Science Letters 249, 484–493.

Hirose, T., Bystricky, M., 2007. Extreme dynamic weakening of faults during dehydration by coseismic shear heating. Geophysical Research Letters 34, L14311.

Janssen, C., Wirth, R., Rybacki, E., Naumann, R., Kemmitz, H., Wenk, H.-R., Dresen, G., 2010. Amorphous material in SAFOD core samples (San Andreas Fault): evidence for crush-origin pseudotachylytes? Geophysical Research Letters 37, L01303.

Janssen, C., Wirth, R., Reinicke, A., Rybacki, E., Naumann, R., Wenk, H.-R., Dresen, G., 2011. Nanoscale porosity in SAFOD core samples (San Andreas Fault). Earth and Planetary Science Letters 301, 179–189.

Jung, H., Green, H.W., 2004. Experimental faulting of serpentinite during dehydration: implications for earthquakes, seismic low-velocity zones and anomalous hypocenter distributions in subduction zones. International Geology Review 46, 1089–1102.

Kennedy, L.A., Logan, J.M., 1998. Microstructures of cataclasites in a limestone-on-shale thrust fault: implications for low-temperature recrystallization of calcite. Tectonophysics 295, 167–186.

Kennedy, L.A., White, J.C., 2001. Low-temperature recrystallization in calcite: mechanisms and consequences. Geology 29, 1027–1030.

Liu, J., Cao, S., 2006. Change of deformation mechanisms during low temperature flow of rocks - observations from micron to nanometer scales. In: Phillipp, S., Leiss, B., Vollbrecht, A., Tanner, D., Gudmundsson, A. (Eds.), Tektonik, Struktur und Kristallingeologie. Universitatsverlag Gottingen, pp. 135–136.

Macaudiere, J., Brown, W.L., Ohnenstetter, D., 1985. Microcrystalline textures resulting from rapid crystallization in a pseudotachylite melt in a meta-anorthosite. Contribution to Mineralogy and Petrology 89, 39–51.

Magloughlin, J.F., 1992. Microstructural and chemical changes associated with cataclasis and frictional melting at shallow crustal levels: the cataclasite-pseudotachylyte connection. Tectonophysics 204, 243–260.

Mair, K., Frye, K.M., Marone, C., 2002. Influence of grain characteristics on the friction of granular shear zones. Journal of Geophysical Research 107, B10–B2219.

McLaren, A.C., 1991. Transmission Electron Microscopy of Minerals and Rocks. Cambridge University Press.

Merriman, R.J., Roberts, B., Peacor, D.R., Hirons, S.R., 1995. Strain-related differences in the crystal growth of white mica and chlorite: a TEM and XRD study of the development of metapelitic microfabrics in the Southern Upland thrust terrane, Scotland. Journal of Metamorphic Geology 13, 559–576.

Mo, Y., Turner, K.T., Szlufarska, I., 2009. Friction laws at the nanoscale. Nature 457, 1116–1119.

Moecher, D.P., Brearley, A.J., 2004. Mineralogy and petrology of a mullite-bearing pseudotachylyte: constraints on the temperature of coseismic frictional fusion. American Mineralogist 89, 1486–1495.

Moore, D.E., Lockner, D.A., Summers, R., Shengli, M., Byerlee, J.D., 1996. Strength of chrysotile-serpentinite gouge under hydrothermal conditions: can it explain a weak San Andreas fault? Geology 24, 1041–1044.

Moore, D.E., Lockner, D.A., Shengli, M., Summers, R., Byerlee, J.D., 1997. Strengths of serpentinite gouges at elevated temperatures. Journal of Geophysical Research 102, 14787–14801.

Moore, D.E., Lockner, D.A., 2004. Crystallographic controls on the frictional behavior of dry and water-saturated sheet structure minerals. Journal of Geophysical Research 109, B03401.

Moore, D.E., Rymer, M.J., 2007. Talc-bearing serpentinite and the creeping section of the San Andreas fault. Nature 448, 795–797.

Moore, D.E., Lockner, D.A., 2008. Talc friction in the temperature range 25°–400 °C: relevance for fault-zone weakening. Tectonophysics 499, 120–132.

Morrow, C.A., Moore, D.E., Lockner, D.A., 2000. The effect of mineral bond strength and adsorbed water on fault gouge frictional strength. Geophysical Research Letters 27, 815–818.

Otsuki, K., Monzawa, N., 2003. Fluidization and melting of fault gouge during seismic slip: identification in the Nojima fault zone and implications for focal earthquake mechanisms. Journal of Geophysical Research 108, B4 2192.

Ozawa, K., Takizawa, S., 2007. Amorphous material formed by mechanochemical effect in natural pseudotachylyte of crushing origin: a case study of the Iida-Matsukawa Fault, Nagano prefecture, central Japan. Journal of Structural Geology 29, 1855–1869.

Peacock, S.M., 2001. Are the lower planes of double seismic zones caused by serpentine dehydration in subducting oceanic mantle? Geology 29, 299–302.

Raleigh, C.B., Paterson, M.S., 1965. Experimental deformation of serpentinites and its tectonic implications. Journal of Geophysical Research 70, 3965–3985.

Reinen, L., Weeks, J.D., Tullis, T.E., 1991. The frictional behaviour of serpentinite: implications for aseismic creep on shallow crustal faults. Geophysical Research Letters 18, 1921–1924.

Reinen, L.A., Weeks, J.D., Tullis, T.E., 1994. The frictional of lizardite and antigorite serpentinites: experiments, constitutive models and implications for natural faults. Pure and Applied Geophysics 143, 317–358.

Rice, J.R., 2006. Heating and weakening of faults during earthquake slip. Journal of Geophysical Research 11, B05311.

Saffer, D.M., Marone, C., 2003. Comparison of smectite and illite-rich gouge frictional properties: applications to the updip limit of the seismogenic zone along subduction megathrusts. Earth and Planetary Science Letters 215, 219–235.

Sammis, C.G., Ben-Zion, Y., 2008. Mechanics of grain-size reduction in fault zones. Journal of Geophysical Research 113, B02306.
Schleicher, A.M., van der Pluijm, B.A., Solum, J.G., Warr, L.N., 2006. Origin and significance of clay-coated fractures in mudrock fragments of the SAFOD borehole (Parkfield, California). Geophysical Research Letters 33, L16313.
Schleicher, A.M., van der Pluijm, B.A., Warr, L., Shahla, A., Stute, M., Torgensen, T., 2010. Mineralogical changes in the active creeping section of the SAFOD borehole in Parkfield, California, and its influence in fault zone weakening processes. Geophysical Research Abstract 12, EGU2010–EGU5252.
Schleicher, A.M., van der, Pluijim, Warr, L.N., 2011. Nanocoatings of clay and creep of the San Andreas fault at Parkfield, California. Geology 38, 667–670.
Sibson, R.H., 1977. Structural permeability of fluid-driven fault-fracture meshes. Journal of Structural Geology 18, 1031–1042.
Solum, J.G., van der Pluijm, B.A., Peacor, D.R., 2003. Influence of phyllosilicate mineral assemblages, fabrics and fluids on the behavior of the Punchbowl fault, southern California. Journal of Geophysical Research 108, B52233.
Solum, J.G., van der Pluijm, B.A., Peacor, D.R., 2005. Neocrystallization, fabrics and age of clay minerals from an exposure of the Moab Fault, Utah. Journal of Structural Geology 27, 1563–1576.
Storti, F., Billi, A., Salvini, F., 2003. Particle size distributions in natural carbonate fault rocks: insights for non-self-similar cataclasis. Earth and Planetary Science Letters 206, 173–186.
Tullis, J., Yund, R.A., 1980. Hydrolitic weakening of experimentally deformed Westerly granite and Hale albite rock. Journal of Structural Geology 2, 439–451.
Ujiie, K., Yamaguchi, H., Sakaguchi, A., Toh, S., 2007. Pseudotachylytes in an ancient accretionary complex and implications for melt lubrication during subduction zone earthquakes. Journal of Structural Geology 29, 599–613.
Van der Pluijm, B.A., Schleicher, A.M., Warr, L.N., 2010. How clays weaken faults. Geophysical Research Abstract 12 EGU2010-6563-1.
Viganò, A., Tumiati, S., Recchia, S., Martin, S., Marelli, M., Rigon, R., 2011. Carbonate Pseudotachylytes: Evidence for Seismic Faulting along Carbonate Faults. Terra Nova. doi:10.1111/j.1365–3121.2011.00997.x.
Viti, C., Collettini, C., 2009. Growth and deformation mechanisms of talc along a natural fault: a micro/nanostructural investigation. Contributions to Mineralogy and Petrology 158, 529–542.
Viti, C., Hirose, T., 2009. Dehydration reactions and micro/nanostructures in experimentally-deformed serpentinites. Contributions to Mineralogy and Petrology 157, 327–338.
Viti, C., Hirose, T., 2010. Thermal decomposition of serpentine during coseismic faulting: nanostructures and mineral reactions. Journal of Structural Geology 32, 1476–1484.
Warr, L.N., van der Pluijm, B.A., Peacor, D.R., Hall, C.M., 2003. Frictional melt pulses during a 1.1 Ma earthquake along the Alpine fault, New Zealand. Earth and Planetary Science Letters 209, 39–52.
Weiss, L.E., Wenk, H.R., 1983. Experimentally produced pseudotachylite-like veins in gabbro. Tectonophysics 96, 299–310.
Wenk, H.R., 1976. Electron Microscopy in Mineralogy. Springer-Verlag, Berlin Heidelberg New York.
Wenk, H.-R., 1978. Are pseudotachylytes products of fracture or fusion? Geology 6, 507–511.
Wibberley, C., 2007. Talc at fault. Nature 448, 756–757.
Wibberley, C., 1999. Are feldspar-to-mica reactions necessarily reaction-softening processes in fault zones? Journal of Structural Geology 21, 1219–1227.
Williams, D.B., Carter, C.B., 1996. Transmission Electron Microscopy. Plenum Press, New York and London.
Wilson, B., Dewers, T., Reches, Z., Brune, J., 2005. Particle size and energetics of gouge from earthquake rupture zones. Nature 434, 749–752.
Wintsch, R.P., Christoffersen, R., Kronenberg, A.K., 1995. Fluid-rock reaction weakening of fault zones. Journal of Geophysical Research 100, 13021–13032.
Wirth, R., 2004. Focused ion beam (FIB): a novel technology for advanced application of micro and nanoanalysis in geosciences and applied mineralogy. European Journal of Mineralogy 16, 863–876.
Yan, Y., van der Pluijim, B.A., Peacor, D.R., 2001. Deformation microfabrics of clay gouge, Lewis Thrust, Canada: a case for fault weakening from clay transformation. In: Geological Society, London Special Publications, vol. 186, pp. 103–112.
Yund, R.A., Blanpied, M.L., Tullis, T.E., Weeks, J.D., 1990. Amorphous material in high strain experimental fault gouges. Journal of Geophysical Research 95, 15589–15602.